

# Revisiting Global Statistics Aggregation for Improving Image Restoration

Xiaojie Chu, Liangyu Chen, Chengpeng Chen, Xin Lu

Megvii Technology  
 {chuxiaojie, chenliangyu, luxin}@megvii.com  
 chencp@live.com

## Abstract

Global spatial statistics, which are aggregated along entire spatial dimensions, are widely used in top-performance image restorers. For example, mean, variance in Instance Normalization (IN) which is adopted by HINet, and global average pooling (i.e. mean) in Squeeze and Excitation (SE) which is applied to MPRNet. This paper first shows that statistics aggregated on the patches-based/entire-image-based feature in the training/testing phase respectively may distribute very differently and lead to performance degradation in image restorers. It has been widely overlooked by previous works. To solve this issue, we propose a simple approach, Test-time Local Statistics Converter (TLSC), that replaces the region of statistics aggregation operation from global to local, only in the test time. Without retraining or finetuning, our approach significantly improves the image restorer’s performance. In particular, by extending SE with TLSC to the state-of-the-art models, MPRNet boost by 0.65 dB in PSNR on GoPro dataset, achieves 33.31 dB, exceeds the previous best result 0.6 dB. In addition, we simply apply TLSC to the high-level vision task, i.e. semantic segmentation, and achieves competitive results. Extensive quantity and quality experiments are conducted to demonstrate TLSC solves the issue with marginal costs while significant gain. The code is available at <https://github.com/megvii-research/tlsc>.

## 1 Introduction

Image restoration is the task of estimating the clean image from a corrupt (e.g. motion blur, noise, etc.) image. Recently, deep learning based models (Yi et al. 2021; Zamir et al. 2021a; Chen et al. 2021a) have achieved state-of-the-art (SOTA) performance in this field, and the global spatial statistics are increasingly indispensable for the top performance restorers: HINet (Chen et al. 2021a) adopts Instance Normalization (IN (Ulyanov, Vedaldi, and Lempitsky 2016)) module which requires mean and variance of the entire spatial dimension. MPRNet (Zamir et al. 2021a), SPDNet (Yi et al. 2021), FFA-Net (Qin et al. 2020), etc. adopt Squeeze and Excitation (SE (Hu, Shen, and Sun 2018)) module which requires mean (i.e. global average pooling in this case) of the entire spatial dimension.

In this paper, we notice the statistics distribution shifts from training to testing may occur and lead to performance

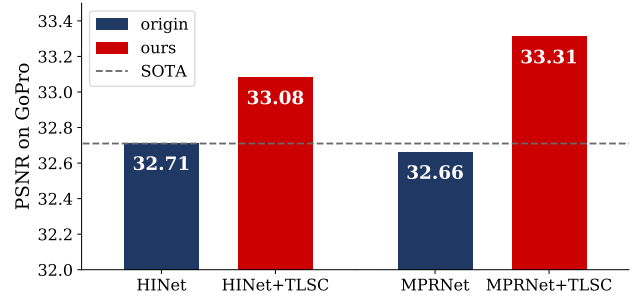


Figure 1: By applying our proposed TLSC to top-performance models on GoPro (Nah, Hyun Kim, and Mu Lee 2017) dataset without retraining, HINet (Chen et al. 2021a) and MPRNet (Zamir et al. 2021b) exceed the previous best result (plotted as black dashed line) 0.37 dB and 0.60 dB, respectively.

degradation in image restoration models. Concretely, statistics are aggregated on the patches-based/entire-image-based feature in the training (see Fig. 2a)/testing (see Fig. 2b) phase, respectively, such as (Qin et al. 2020; Yi et al. 2021; Zamir et al. 2021a). The entire-image-based statistics may distribute very differently from the patches-based statistics. The shifts in the statistics distribution in training and testing may lead to performance drops, and it has been widely overlooked by previous works.

Intuitively, there are some alternatives that may mitigate it. One approach is cropping the image into patches and predict the result independently (see in Fig. 2c). It can alleviate the patches/full-image inconsistency issue described above, while it induces unsmoothness of the boundary (i.e. “boundary artifacts” as demonstrated in (Lee 2015)). Another straightforward approach is training with full-sized images. But it damages the performance although avoids the inconsistency.

To solve the drawbacks of the above approaches, we proposed a novel approach, Test-time Local Statistics Converter (TLSC). It reduces statistics distribution shifts between training and testing *without retraining or finetuning*. Specifically, as shown in Fig. 2d, by testing with the full image (thus reduces boundary artifacts), TLSC aggregates

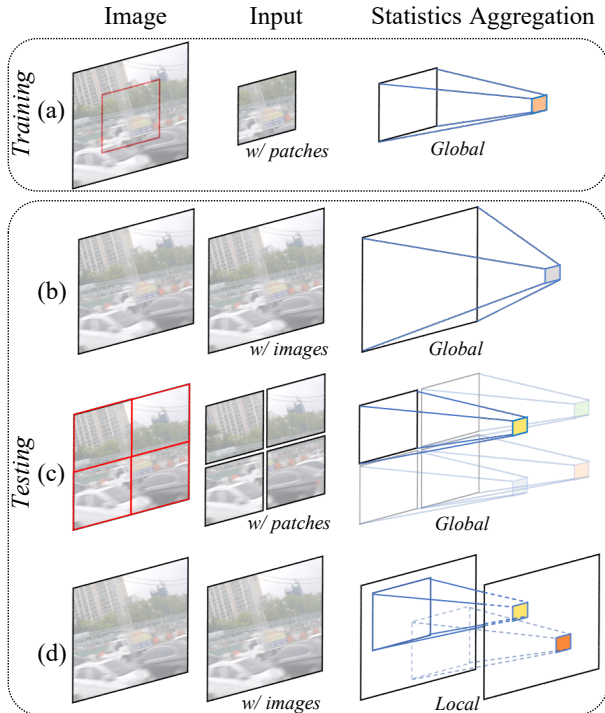


Figure 2: Illustration of training and testing schemes of image restoration. From left to right: image from the dataset; input for the restorer (patches or entire-image depend on the scheme); aggregating statistics from the feature map. For (a), (b), and (c), statistics are aggregated along the entire spatial dimension. (d) Ours, statistics are aggregated in a local region for each pixel.

statistics in a local region for each pixel instead of aggregating statistics along the entire spatial dimension: the statistics distribution is close to that during training although inference by the full image.

TLSC can be easily extended to existing modules, as no retraining or finetuning are required. To show the effectiveness of our proposed TLSC, we extend it to the modules, e.g. IN/SE. We mainly evaluate our approach on datasets with large training/testing spatial gaps (e.g. GoPro (Nah, Hyun Kim, and Mu Lee 2017), REDS (Nah et al. 2019), HIDE (Shen et al. 2019), etc.) Extensive experiments are conducted on various datasets and tasks demonstrate the effectiveness of TLSC. In particular, as we show in Fig. 1 and Tab. 3a, MPRNet-local (by extending the SE in MPRNet with TLSC) achieves 33.31 (+0.65) dB PSNR on GoPro with 0.16% extra MACs, HINet-local (by extending the IN in HINet with TLSC) achieves 33.08 (+0.37) dB PSNR on GoPro with nearly extra cost-free. Besides, we extend TLSC to high-level vision task, i.e. semantic segmentation without bells and whistles, and achieves competitive results.

Our contributions can be summarized as follows:

- To the best of our knowledge, we are the first to point out the inconsistency of the statistics distribution in training (by image patches) and testing (by the full image) in

image restoration tasks, which may degrade the performance badly.

- To practically reduce the statistics distribution shifts between training and testing, we analyze the drawbacks of existing approaches and propose Test-time Local Statistics Converter (TLSC). Without retraining or finetuning, TLSC replaces the statistics aggregation operation from global to local, significantly improves performance with nearly cost-free by reducing the train-test inconsistency.
- By extending TLSC to the modules (i.e. IN and SE) in various models, their performances are considerably improved. It demonstrates our proposed approach is practical and effective.
- In addition, extensive experiments are conducted to demonstrate the effectiveness of our proposed approach. We also do quantity and quality experiments to demonstrate our proposed approach improving performance by reducing statistics inconsistency in training and testing.

## 2 Related Work

**Image Restoration** Image Restoration tasks, e.g. denoising, deblurring, deraining, dehazing, etc. aim to restore the degraded image to the clean one. Deep learning based restoration models have achieved state-of-the-art results (Yi et al. 2021; Zamir et al. 2021a; Chen et al. 2021a) recently. The training data are cropped into patches and fed into the model in the training phase. Most methods (Qin et al. 2020; Yi et al. 2021; Zamir et al. 2021a) inference by the full image for testing, which leads to a training/testing inconsistency problem. HINet (Chen et al. 2021a) crops the image into patches for prediction, which would result in boundary artifacts as (Lee 2015) demonstrated.

**Spatial Statistics in Image Restoration Models** Channel attention mechanism is introduced by SENet (Hu, Shen, and Sun 2018), it infers channel-wise attention using global average-pooled (i.e. the mean of the spatial dimension) features. SE or SE-based methods, such as CBAM (Woo et al. 2018) have been successfully adopted to image restoration models. For example, (Li et al. 2018b; Yi et al. 2021) for deraining, (Suin, Purohit, and Rajagopalan 2020; Zamir et al. 2021a) for deblurring, (Zhang et al. 2018) for super-resolution, (Anwar and Barnes 2019; Zamir et al. 2020) for denoising and (Qin et al. 2020) for dehazing.

Besides, HINet (Chen et al. 2021a) introduces Instance Normalization (IN (Ulyanov, Vedaldi, and Lempitsky 2016)) to image restoration tasks, which normalizes each channel of the features by its mean and variance. The performance growth brings by IN once again proves the effectiveness of spatial statistics.

In this paper, we mainly discuss these modules, which aggregate the statistics from the entire spatial dimension (i.e. globally), as representatives. We find that the performance of these modules may degrade due to the training/testing inconsistency mentioned above.

**Local Spatial Statistics Modules** In local spatial schemes, the statistics are computed within a local spatial area for each pixel. Local Response Normalization

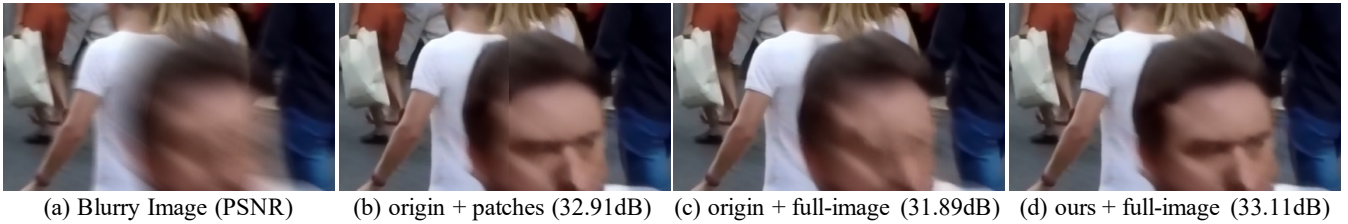


Figure 3: Crops of visualized deblurring results of MPRNet (Zamir et al. 2021b) on GoPro (Nah, Hyun Kim, and Mu Lee 2017) generated by different testing schemes. (b) Test with patches, i.e. Fig. 2c; (c) Test with images, i.e. Fig. 2b; (d) Test with images and TLSC is adopted (ours), i.e. Fig. 2d. It illustrates that (d) provides sharp results while avoids the boundary artifacts in (b).

(LRN) (Lyu and Simoncelli 2008; Jarrett et al. 2009; Krizhevsky, Sutskever, and Hinton 2012) computes the statistics in a small neighborhood for each pixel. Positional Normalization (Li et al. 2019) only normalizes over a single spatial position at a time. Local Context Normalization (LCN) (Ortiz et al. 2020) normalizes every point of features based on a window around it and the filters in its group, and so does the Local Feature Normalization Layer (Kotovenko et al. 2019). Gather-excite (GE (Hu et al. 2018)) module generalizes the squeeze operation (global average pooling) and support gather the statistics locally. For semantic image synthesis tasks, SPatially-Adaptive (DE)normalization (SPADE) (Park et al. 2019) utilize the input semantic layout for modulating the activations through a spatially-adaptive, learned transformation. Region Normalization (RN) (Yu et al. 2020), a spatial region-wise normalization, is proposed for better inpainting network training.

However, directly applying those modules to existing restoration models is not practical, as retraining or finetuning are required. Besides, these modules are designed to supplement context information, thus it utilizes local statistics in both the training and testing phase, which does not solve the inconsistency issue. Conversely, our proposed approach does not need to retrain or finetune the model, and the local statistics are only utilized in inference to solve the inconsistency issue.

### 3 Approach

In this section, we first introduce the image restoration pipeline and the statistics inconsistency induced by it, and discuss why can't existing methods solve this problem well. Next, in order to solve the inconsistency, we illustrate our novel approach, Test-time Local Statistics Converter (TLSC), and the details of extending TLSC to existing modules.

**Image Restoration Pipeline** We briefly describe the image restoration pipeline used in the SOTA methods. For practical application, datasets are usually composed of high-resolution images. But in the training stage, it will be used as the training data *after crop*, see Fig. 2a, as full-image training causes severe performance loss, as shown in Tab. 1. In testing, the full image is proposed for inference, as shown in Fig. 2b.

**Spatial Statistics Aggregation** Spatial statistics (referred to as “statistics” for simplicity) have verified its effectiveness in the SOTA image restorers (Yi et al. 2021; Zamir et al. 2021a; Chen et al. 2021a). The (global) statistics aggregation of a feature layer  $\mathbf{X} \in \mathbb{R}^{H \times W}$  (without loss of generality, we ignore the channel dimension), can be formulated as:

$$\Phi(\mathbf{X}, f) = \frac{1}{HW} \sum_{p=1}^H \sum_{q=1}^W f(\mathbf{X}_{p,q}). \quad (1)$$

where  $f : \mathbb{R} \rightarrow \mathbb{R}$  defines how statistics are calculated, and  $\Phi(\mathbf{X}, f) \in \mathbb{R}$  denotes the aggregated statistics. It's computational complexity is  $\mathcal{O}(HW)$ .

**Statistics Distribution Inconsistency** In training, parameters are optimized by the patches-based statistics. While in testing, the layer inference the results by the entire-image-based statistics. However, statistics distribution discrepancy occurs, see Fig. 4a. It is hard for restorers to adapt to the severe changes in statistics distribution, resulting in performance degradation, as we demonstrated in Sec. 4.2.

**Discussion on Existing Methods** Dividing the image into patches for inference can avoid the path/entire-image inconsistency. However, it introduced a new issue, boundary artifacts (Lee 2015). URST (Chen et al. 2021b) simulates the full-image-testing scheme with patches by replacing the patch statistics with the full image statistics but it may lead to performance degradation as the patch/entire-image inconsistency described above.

#### 3.1 Test-time Local Statistics Converter

Based on the inconsistency issue and the drawbacks discussed above, we can summarize a practical solution that should take the following conditions into account,

1. To be widely adopted, it should effect without retraining or finetuning. In this case, the solution could be conveniently applied to already trained models.
2. The statistics distribution should match in train and test. Otherwise, performance degradation occurs.
3. To maintain image quality, obvious boundary artifacts cannot be introduced.
4. It should not induce a computational bottleneck. Otherwise, practical applications will ignore the solution.

Next, we discuss the above four conditions. Due to the first condition, the solution should only take effect during the test phase. It limits us to design a test-time solution based on the trained models and satisfy the remaining conditions at the same time. The second condition could be accomplished by dividing the image into patches and inference them independently as in HINet (Chen et al. 2021a), while it violates the third condition.

Inspired by the patch-testing scheme and avoiding its shortcomings, we propose a test-time solution: 1) full-image as input to reduce the boundary artifacts, 2) each pixel in the feature map aggregates its own statistics in a local window, as shown in Fig. 2d. As a result, the scope of each pixel’s statistics is limited to the window, which is consistent with training (Fig. 2a). It implies the statistics aggregation operation scope converts from global to local.

Formally, each pixel *e.g.*  $(i, j)$  aggregates the statistics in a local window (size  $K_h \times K_w$ ) of feature  $\mathbf{X} \in \mathbb{R}^{H \times W}$  could be formulated as:

$$\Psi(\mathbf{X}, f)_{i,j} = \frac{1}{K_h K_w} \sum_p \sum_q f(\mathbf{X}_{p,q}), \quad (2)$$

where  $(p, q)$  in the local window of  $(i, j)$ ,  $\Psi(\mathbf{X}, f) \in \mathbb{R}^{H \times W}$  indicates the aggregated local statistics, and  $K_h, K_w$  are hyperparameters.

The edge case, *eg.*  $(i, j)$  is the boundary of  $\mathbf{X}$ , is not considered above for simplicity. In practice, we implement  $\Psi(\mathbf{X}, f)$  by two steps. First, sliding windows (size of  $K_h \times K_w$ ) with stride equals 1 to aggregate the local statistics for each pixel in non-edge case. Second, padding the result by replication of its boundary for edge case. The first step’s computational complexity is  $\mathcal{O}(HWK_h K_w)$ . But mean/sum statistics aggregation within each local window could be treated as *submatrix sum* problem and solved by prefix sum trick (Harris, Sengupta, and Owens 2007) with  $\mathcal{O}(1)$  complexity (Amir, Church, and Dar 2004). Therefore, the overall complexity could be reduced to  $\mathcal{O}(HW)$  which is consistent with global statistics aggregation operation, *i.e.* Eq.(1). It demonstrates that we meet the fourth condition.

In conclusion, our test-time solution can be summarized as converting the statistics aggregation operation from global to local, *i.e.* each pixel of the feature aggregates its own statistics locally. Therefore, we name it Test-time Local Statistics Converter (TLSC).

### 3.2 Extending TLSC to existing modules

In this subsection, we borrow the notations defined above (*e.g.*  $\Phi/\Psi$  for global/local statistics aggregation operation, respectively). To extend TLSC to existing modules, we convert the statistics aggregation operation from global (*i.e.*  $\Phi$ ) to local (*i.e.*  $\Psi$ ). In the following, we take Squeeze-and-Excitation(SE) and Instance Normalization(IN) as representatives, and it can be easily applied to other normalization modules such as Group Normalization (GN (Wu and He 2018)) or variants of SE (*e.g.* CBAM (Woo et al. 2018), GE (Hu et al. 2018)).

**Extending TLSC to SE Block** We briefly revisit the squeeze-and-excitation (SE (Hu, Shen, and Sun 2018))

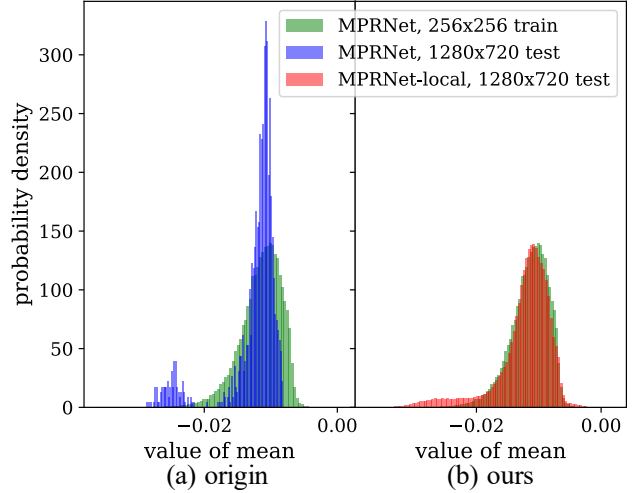


Figure 4: Visualization of the statistics (mean) distribution of the first SE layer of the second encoder in MPRNet on GoPro dataset. Green: the distribution when training with patches; Blue: the distribution when testing with images; Red: the distribution when testing with images and TLSC is adopted (denoted as MPRNet-local). (a) The original test scheme results in distribution shifts. (b) Distribution shifts could be reduced by our proposed TLSC.

block first. For a feature map  $\mathbf{X} \in \mathbb{R}^{H \times W \times C}$  with a spatial size of  $(H, W)$  and  $C$  channels, SE block first squeezes the global spatial information into channels, it could be denoted as  $\Phi(\mathbf{X}^{(c)}, id), \forall c \in [C]$ , where  $id(t) = t, \forall t \in \mathbb{R}$ . And then, a multilayer perceptron (MLP) follows to evaluate the channel attention, which re-weights the feature map.

The squeeze on the global spatial dimension could be sub-optimal as statistics distribution shifts. To solve this, we extend TLSC to SE by replacing  $\Phi(\mathbf{X}^{(c)}, id)$  to  $\Psi(\mathbf{X}^{(c)}, id), \forall c \in [C]$ . As in SE, an MLP along the channel dimension follows. Differently, the feature map is re-weighted by the element-wise attention in this case.

**Extending TLSC to IN Block** For a feature map  $\mathbf{X} \in \mathbb{R}^{H \times W}$  (we omit the channel dimension for simplicity), the normalized feature  $\mathbf{Y}$  is computed as:

$$\mathbf{Y} = \frac{\mathbf{X} - \mu}{\sigma}, \quad (3)$$

where statistics  $\mu$  and  $\sigma$  are the mean and variance computed over the global spatial of  $\mathbf{X}$ :

$$\begin{aligned} \mu &= \Phi(\mathbf{X}, id), \\ \sigma^2 &= \Phi(\mathbf{X}, sq) - \mu^2, \end{aligned} \quad (4)$$

where  $id(t) = t, sq(t) = t^2, \forall t \in \mathbb{R}$ . Besides, learnable parameters  $\gamma, \beta$  are used to scale and shift the normalized feature  $\mathbf{Y}$ , we omit them for simplicity.

In inference we can extend TLSC to IN by replacing  $\Phi(\mathbf{X}, id)$  and  $\Phi(\mathbf{X}, sq)$  in Eq.(4) to their local version:

$$\begin{aligned} \mu_{local} &= \Psi(\mathbf{X}, id), \\ \sigma_{local}^2 &= \Psi(\mathbf{X}, sq) - \mu_{local}^2, \end{aligned} \quad (5)$$

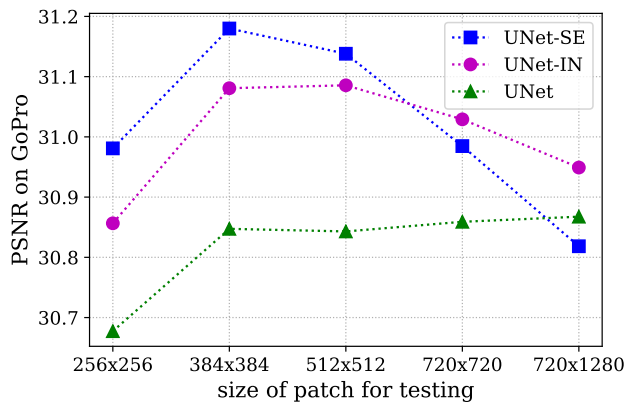


Figure 5: Image deblurring performance of UNet, UNet-SE, and UNet-IN on GoPro dataset at different sizes of patch for testing. In contrast to UNet, the performance of UNet-SE/UNet-IN decreases when size of patch for testing increases from  $512 \times 512$ .

where  $\mu_{local}, \sigma_{local} \in \mathbb{R}^{H \times W}$  indicate the statistics aggregated along each position. The normalized feature  $\mathbf{Y}_{local}$  could be represent as:

$$\mathbf{Y}_{local} = \frac{\mathbf{X} - \mu_{local}}{\sigma_{local}}. \quad (6)$$

## 4 Experiments

In this section, we do quality and quantity experiments to show the effects of train-test inconsistency, and our proposed approach Test-time Local Statistics Converter (TLSC) can reduce this inconsistency. Next, the extensibility of TLSC and the choice of hyperparameters are discussed.

### 4.1 Implementation details

**Architecture** We use a simple UNet model (i.e. HINet Simple (Chen et al. 2021a) without HIN) as baseline (denoted as UNet). Attention modules (e.g., SE (Hu, Shen, and Sun 2018), GE- $\theta^-$  (Hu et al. 2018) and CBAM (Woo et al. 2018)) are added to UNet encoder following (Hu, Shen, and Sun 2018) (denoted as UNet-SE, UNet-GE- $\theta^-$  and UNet-CBAM respectively), while Normalization modules (e.g., IN (Ulyanov, Vedaldi, and Lempitsky 2016) and GN (Wu and He 2018)) are added to the UNet following (Chen et al. 2021a) (denoted as UNet-IN and UNet-GN respectively).

**Dataset** The GoPro (Nah, Hyun Kim, and Mu Lee 2017) dataset for deblurring, which contains 2103 image pairs for training and 1111 pairs for evaluation, is used in this section for training and testing.

**Training** We follow the most training detail of HINet Simple (Chen et al. 2021a). Specially, the default size of patches for training is  $256 \times 256$ , and the default batch size is 64. We also use the warm-up strategy in the first 5000 iterations. When training with different patch sizes, we keep the total number of pixels seen by the model during training the same

| Model   | train w/ patches | train w/ full-images |
|---------|------------------|----------------------|
| UNet    | 30.87            | 30.20 (-0.67)        |
| UNet-SE | 30.82            | 30.51 (-0.31)        |
| UNet-IN | 30.89            | 30.39 (-0.50)        |

Table 1: The performance (PSNR) of UNet, UNet-SE, and UNet-IN decrease significantly when training with full images on GoPro dataset.

as the default configuration for a fair comparison, and hyperparameters are adjusted based on experimental trials. Details of the training are in the supplementary material.

**Testing** We use MACs (i.e. multiplier-accumulator operations) to evaluate the computational cost of models, which is estimated when the input is  $512 \times 512$ . To determinate the hyperparameter, i.e. local window size of each layer (which aggregates the statistics) as we mentioned in Sec.3.1, we propose a simple strategy: A calibration image is fed into the model, and the spatial sizes of these feature layers are recorded as their local window size. Therefore, the hyperparameter could be determined by the spatial size of the calibration image, and we denoted the image size as “local window size” for simplicity in the following. Besides, the calibration could be accomplished offline, thus does not increase the test latency. The local window size is set to  $384 \times 384$  by default, and we will discuss the impact of this hyperparameter in the Sec. 4.4.

### 4.2 Train-Test Inconsistency

**Statistics Distribution Shifts and Its Consequences** To analyze the effects of train-test inconsistency, we compare the statistics based on patches and full-images, which are aggregated by the first SE layer of the second encoder in MPRNet (Zamir et al. 2021a). As shown in Fig. 4a, the statistics distribution shifts from training (green) to testing (blue).

To demonstrate that the inconsistency further results in performance degradation, we conduct experiments on UNet, UNet-IN, and UNet-SE. By testing with various patch sizes, statistics-dependent models, i.e. UNet-IN and UNet-SE, behave differently from UNet, as shown in Fig. 5. Specifically, with the increasing size of patches for testing, the performance increases in the case of UNet while it increases and then *decreases* in UNet-IN and UNet-SE cases. We conjecture the model could utilize more information based on a larger patch for testing; thus, UNet (green) achieves better performance. However, statistics-dependent models, i.e. UNet-SE (blue) and UNet-IN (purple), not only benefit from the increasing patch size like UNet does but also suffer performance damage due to inconsistent statistics. This is because the gap of training and testing patch size increases. As a result, performance degradation occurs at UNet-SE and UNet-IN when patch size is larger than  $384 \times 384$ . Besides, the  $384 \times 384$  achieves the best result for UNet-SE and UNet-IN. We attribute it to the suitable larger patch for testing while inducing only minor statistics distribution shifts.

**Possible Solutions and Their Drawbacks** Dividing the image into patches for inference may alleviate the inconsis-

| Model               | TLSC | PSNR          | MACs(G)       |
|---------------------|------|---------------|---------------|
| UNet-IN             | ✓    | 30.95         | 62.13         |
|                     |      | 31.11 (+0.16) | 62.13 (+0.00) |
| UNet-GN             | ✓    | 30.91         | 62.13         |
|                     |      | 31.03 (+0.12) | 62.13 (+0.00) |
| UNet-GE- $\theta^-$ | ✓    | 30.74         | 62.14         |
|                     |      | 30.91 (+0.17) | 62.14 (+0.00) |
| UNet-SE             | ✓    | 30.82         | 62.14         |
|                     |      | 31.21 (+0.39) | 62.19 (+0.05) |
| UNet-CBAM           | ✓    | 30.53         | 62.19         |
|                     |      | 31.05 (+0.52) | 62.27 (+0.08) |

Table 2: The results of applying TLSC to SE (Hu, Shen, and Sun 2018), IN (Ulyanov, Vedaldi, and Lempitsky 2016), GN (Wu and He 2018), GE- $\theta^-$  (Hu et al. 2018) and CBAM (Woo et al. 2018) modules on GoPro dataset. TLSC improves the performance of all models with marginal costs.

tency issue, e.g.  $384 \times 384$  patch size in Fig. 5 achieves competitive results. However, as shown in Fig. 3b, “boundary artifacts” is introduced (Lee 2015) which severely damages the image quality. Another straightforward idea to bridge the gap in statistics between training and testing is training by full-images, but it leads to significant performance degradation. As shown in Tab. 1, PSNR of UNet, UNet-SE, and UNet-IN decrease 0.67 dB, 0.31 dB, and 0.50 dB, respectively. This is explained by that full-images training lacks cropping augmentation. In a word, the above approaches can not improve the performance of models.

**Effectiveness of TLSC** We conduct quality and quantity experiments to demonstrate the effectiveness of TLSC. Concretely, we apply TLSC to MPRNet (denoted as MPRNet-local) such that it aggregates statistics locally (instead of globally) in inference. It ensures the statistics aggregation region be consistent with training, as demonstrated in Fig. 2a and Fig. 2d. The statistics distribution shifts are reduced by TLSC as shown in Fig. 4b compares to Fig. 4a: the statistics distribution obtained by our MPRNet-local (red) is close to the original MPRNet in the training phase (green). Besides, as shown in Fig. 3d, boundary artifacts is reduced.

In addition, as shown in Tab. 2, by applying TLSC to UNet-IN and UNet-SE, the performances (i.e. PSNR) boost by 0.16/0.39 dB and achieves 31.11/31.21 dB respectively. The PSNR beyond the baseline (i.e. UNet, green dashed line in Fig. 5) a considerable margin (31.11/31.21 dB vs. 30.86 dB), this indicates TLSC can improving performance by reducing statistics distribution shifts.

### 4.3 Extensibility

As we describe in Sec. 3.2, TLSC can be easily extended to existing models without retraining. In this subsection, we apply TLSC to various statistics-dependent models (e.g. UNet-IN, UNet-SE etc.), as shown in Tab. 2. Our approach achieves performance gains with marginal costs. In detail, for UNet-IN, UNet-GN, and UNet-GE- $\theta^-$ , TLSC improves the performance (i.e. PSNR) by 0.16 dB, 0.12 dB, and 0.17 dB, respectively, with nearly extra cost-free. For UNet-SE

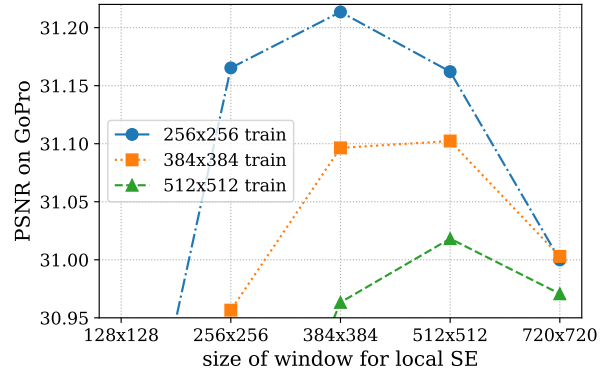


Figure 6: The performance of UNet-SE with different size of local window for TLSC under different training size. The optimal local window size is related to the training size.

and UNet-CBAM, TLSC boosts the performance (i.e. PSNR) by 0.39 dB and 0.52 dB respectively with less than 0.2% extra MACs. It demonstrates the extensibility of TLSC.

### 4.4 Size of Local Window

Size of local window is a hyper-parameter for TLSC, which controls the scope of local statistics aggregation operation. Based on the patch-testing results in Fig. 5 that  $384 \times 384$  patch size for testing achieves better performance than  $256 \times 256$ , although the latter is equal to the training patch size. It could be inferred naturally that it might be sub-optimal to keep the hyper-parameter consistent with training size in all cases. Therefore, we apply TLSC on UNet-SE and conduct experiments on it to illustrate the relation between training patch size and the optimal size of local window, as shown in Fig. 6. Interestingly, the optimal window size for the test phase is not exactly equal but may be larger than the training patch size. We conjecture this is caused by the trade-off between the benefits of more information provided by the larger window and the side-effects of statistic inconsistency between training and testing, as we discussed in Sec. 4.2. In addition, since our approach does not require retraining, it is easy and flexible to tune the size of local window.

## 5 Applications

### 5.1 Image Restoration

To verify the effectiveness of the proposed TLSC, we apply it to various existing top-performing models for image restoration. According to Sec. 4.4, the local window size is set to  $384 \times 384$  if not specified. We report the standard metrics in image restoration, including Peak Signal to Noise Ratio (PSNR), Structural SIMilarity index (SSIM). Since TLSC is designed for solving statistics distribution inconsistency between training and testing, we select the tasks and benchmarks that may lead to this inconsistency. We use the already trained models (if publicly available) with statistics aggregation operations (e.g. SE, IN) and directly apply proposed TLSC to them without any extra re-training.

| Method       | GoPro |       | HIDE  |       | REDS  |       | MACs(G) |
|--------------|-------|-------|-------|-------|-------|-------|---------|
|              | PSNR  | SSIM  | PSNR  | SSIM  | PSNR  | SSIM  |         |
| HINet        | 32.71 | 0.959 | 30.33 | 0.932 | 28.83 | 0.863 | 682.7   |
| HINet-local  | 33.08 | 0.962 | 30.66 | 0.936 | 28.96 | 0.865 | 682.7   |
| MPRNet       | 32.66 | 0.959 | 30.96 | 0.939 | 28.67 | 0.861 | 3106.8  |
| MPRNet-local | 33.31 | 0.964 | 31.19 | 0.942 | 28.95 | 0.865 | 3112.9  |

(a) Deblurring results of HINet (Chen et al. 2021a) and MPRNet (Zamir et al. 2021a) on GoPro (Nah, Hyun Kim, and Mu Lee 2017), HIDE (Shen et al. 2019) and REDS (Nah et al. 2019) datasets.

| Method       | PSNR  | SSIM  | MACs(G) |
|--------------|-------|-------|---------|
| SPDNet       | 43.50 | 0.988 | 386.0   |
| SPDNet-local | 43.70 | 0.989 | 395.8   |

(b) Deraining results of SPDNet (Yi et al. 2021) on SPA-Data (Wang et al. 2019) dataset.

| Method       | SOTS(indoor) |       | SOTS(outdoor) |       | MACs(G) |
|--------------|--------------|-------|---------------|-------|---------|
|              | PSNR         | SSIM  | PSNR          | SSIM  |         |
| FFANet       | 36.39        | 0.989 | 33.57         | 0.984 | 1152.3  |
| FFANet-local | 36.43        | 0.989 | 33.99         | 0.985 | 1152.8  |

(c) Dehazing results of FFANet (Qin et al. 2020) on Synthetic Objective Testing Set (SOTS) from RESIDE (Li et al. 2018a) dataset.

Table 3: Results of various image restoration tasks. Models with TLSC are denoted with *-local* suffix. TLSC is effective in different models and different image restoration tasks without retraining or finetuning.

**Deblurring** We integrate our TLSC with existing top-performing models (e.g. HINet (Chen et al. 2021a) and MPRNet (Zamir et al. 2021a)) and evaluate them on test set of GoPro (Nah, Hyun Kim, and Mu Lee 2017), HIDE (Shen et al. 2019) and REDS (Nah et al. 2019) dataset. As shown in Table 3a, the performance of both HINet and MPRNet are improved by our approach with marginal computational cost. It is worth emphasizing that our approach does not require any re-training or fine-tune. Our models achieve new state-of-the-art results on all three datasets.

In detail, the PSNR on GoPro of HINet and MPRNet are improved by 0.37 dB and 0.65 dB, respectively. And our MPRNet-local exceeds the previous best result (i.e. HINet (Chen et al. 2021a)) by 0.60 dB. The PSNR on HIDE of HINet and MPRNet are improved by 0.33 dB and 0.23 dB, respectively. And our MPRNet-local exceeds the previous best result (i.e. MPRNet (Zamir et al. 2021a)) by 0.23 dB. The PSNR on REDS of HINet and MPRNet are improved by 0.13 dB and 0.28 dB, respectively.

**Deraining** We compare the deraining results of SPDNet (Yi et al. 2021) and our SPDNet-local on SPA-Data (Wang et al. 2019) benchmark. As shown in Table 3b, our approach brings 0.2 dB improvement to SPDNet.

**Dehazing** We compare the dehazing results of FFANet (Qin et al. 2020) and our FFANet-local on Synthetic Objective Testing Set (SOTS) from RESIDE (Li et al. 2018a) dataset. The local window size is set to  $480 \times 480$  and  $416 \times 416$  for SOTS (indoor) and SOTS (outdoor) respectively. As shown in Table 3c, our approach brings 0.04 dB and 0.42 dB improvement to FFANet in indoor and outdoor scenarios, respectively.

Since GoPro (Nah, Hyun Kim, and Mu Lee 2017) / REDS (Nah et al. 2019) / HIDE (Shen et al. 2019), SPA-Data (Wang et al. 2019) and SOTS from RESIDE (Li et al. 2018a) are different image restoration task datasets, it suggests that our proposed TLSC is effective for improving performance of models with global statistics aggregation operations in different image restoration tasks.

| Method        | mIoU  |         | MACs(G) |
|---------------|-------|---------|---------|
|               | ss    | ms+flip |         |
| CGNet         | 68.27 | 70.33   | 27.46   |
| CGNet-local   | 69.38 | 71.93   | 27.92   |
| ResNeSt       | 79.62 | 80.27   | 2094.29 |
| ResNeSt-local | 80.82 | 81.86   | 2125.41 |

Table 4: Semantic segmentation results of CGNet (Wu et al. 2020) and ResNeSt (Zhang et al. 2020) on the Cityscapes (Cordts et al. 2016) val set. Models with TLSC are denoted with *-local* suffix. *ss* and *ms+flip* represent single-scale evaluation and multi-scale evaluation with flipping, respectively.

## 5.2 Semantic Segmentation

Beyond image restoration tasks, training with patches while testing with full-images is also used in semantic segmentation tasks by existing models (Contributors 2020), which may also lead to train-test inconsistency. To test the effect of TLSC, we apply it to two backbones (CGNet (Wu et al. 2020) and ResNeSt (Zhang et al. 2020)) and the performances are reported using the commonly mean Intersection-over-Union (mIoU) on Cityscapes (Cordts et al. 2016) validation set. We utilize the implementation and public available checkpoints from mmsegmentaion (Contributors 2020). The local window size of TLSC is set to  $512 \times 1024$ , which is equal to the size of the patch used for training. As shown in Tab. 4, our TLSC improves the mIoU of all models by more than 1.11% with less than 2% extra MACs. This indicates that our approach is also effective in segmentation tasks.

## 6 Conclusion

In this work, we reveal the statistics distribution shifts issue in image restoration models, which hinders the top-performance restorers. To solve this, we propose Test-time Local Statistics Converter which replaces the statistic aggregation region from the entire spatial dimension to the local window to mitigate the issue between training and testing.

Our approach has no requirement of retraining or finetuning, and only induces marginal extra costs. We demonstrate its efficacy by extensive experiments on various tasks.

## References

- Amir, A.; Church, K. W.; and Dar, E. 2004. The submatrices character count problem: an efficient solution using separable values. *Information and Computation*, 190(1): 100–116.
- Anwar, S.; and Barnes, N. 2019. Real image denoising with feature attention. In *Proceedings of the IEEE/CVF International Conference on Computer Vision*, 3155–3164.
- Chen, L.; Lu, X.; Zhang, J.; Chu, X.; and Chen, C. 2021a. HINet: Half Instance Normalization Network for Image Restoration. In *IEEE/CVF Conference on Computer Vision and Pattern Recognition Workshops*.
- Chen, L.-C.; Zhu, Y.; Papandreou, G.; Schroff, F.; and Adam, H. 2018. Encoder-Decoder with Atrous Separable Convolution for Semantic Image Segmentation. In *ECCV*.
- Chen, Z.; Wang, W.; Xie, E.; Lu, T.; and Luo, P. 2021b. Towards Ultra-Resolution Neural Style Transfer via Thumbnail Instance Normalization. *arXiv preprint arXiv:2103.11784*.
- Contributors, M. 2020. MMSegmentation: OpenMMLab Semantic Segmentation Toolbox and Benchmark. <https://github.com/open-mmlab/mms Segmentation>.
- Cordts, M.; Omran, M.; Ramos, S.; Rehfeld, T.; Enzweiler, M.; Benenson, R.; Franke, U.; Roth, S.; and Schiele, B. 2016. The Cityscapes Dataset for Semantic Urban Scene Understanding. In *Proc. of the IEEE Conference on Computer Vision and Pattern Recognition (CVPR)*.
- Harris, M.; Sengupta, S.; and Owens, J. D. 2007. Parallel prefix sum (scan) with CUDA. *GPU gems*, 3(39): 851–876.
- He, K.; Zhang, X.; Ren, S.; and Sun, J. 2016. Deep residual learning for image recognition. In *Proceedings of the IEEE conference on computer vision and pattern recognition*, 770–778.
- Hu, J.; Shen, L.; Albanie, S.; Sun, G.; and Vedaldi, A. 2018. Gather-excite: Exploiting feature context in convolutional neural networks. *arXiv preprint arXiv:1810.12348*.
- Hu, J.; Shen, L.; and Sun, G. 2018. Squeeze-and-excitation networks. In *Proceedings of the IEEE conference on computer vision and pattern recognition*, 7132–7141.
- Jarrett, K.; Kavukcuoglu, K.; Ranzato, M.; and LeCun, Y. 2009. What is the best multi-stage architecture for object recognition? In *2009 IEEE 12th international conference on computer vision*, 2146–2153. IEEE.
- Kotovenko, D.; Sanakoyeu, A.; Ma, P.; Lang, S.; and Ommer, B. 2019. A content transformation block for image style transfer. In *Proceedings of the IEEE/CVF Conference on Computer Vision and Pattern Recognition*, 10032–10041.
- Krizhevsky, A.; Sutskever, I.; and Hinton, G. E. 2012. Imagenet classification with deep convolutional neural networks. *Advances in neural information processing systems*, 25: 1097–1105.
- Lee, N.-Y. 2015. Block-iterative Richardson-Lucy methods for image deblurring. *EURASIP Journal on Image and Video Processing*, 2015(1): 1–17.
- Li, B.; Ren, W.; Fu, D.; Tao, D.; Feng, D.; Zeng, W.; and Wang, Z. 2018a. Benchmarking single-image dehazing and beyond. *IEEE Transactions on Image Processing*, 28(1): 492–505.
- Li, B.; Wu, F.; Weinberger, K. Q.; and Belongie, S. 2019. Positional normalization. *arXiv preprint arXiv:1907.04312*.
- Li, X.; Wu, J.; Lin, Z.; Liu, H.; and Zha, H. 2018b. Recurrent squeeze-and-excitation context aggregation net for single image deraining. In *Proceedings of the European Conference on Computer Vision (ECCV)*, 254–269.
- Loshchilov, I.; and Hutter, F. 2016. Sgdr: Stochastic gradient descent with warm restarts. *arXiv preprint arXiv:1608.03983*.
- Lyu, S.; and Simoncelli, E. P. 2008. Nonlinear image representation using divisive normalization. In *2008 IEEE Conference on Computer Vision and Pattern Recognition*, 1–8. IEEE.
- Nah, S.; Baik, S.; Hong, S.; Moon, G.; Son, S.; Timofte, R.; and Mu Lee, K. 2019. Ntire 2019 challenge on video deblurring and super-resolution: Dataset and study. In *Proceedings of the IEEE/CVF Conference on Computer Vision and Pattern Recognition Workshops*, 0–0.
- Nah, S.; Hyun Kim, T.; and Mu Lee, K. 2017. Deep multi-scale convolutional neural network for dynamic scene deblurring. In *Proceedings of the IEEE conference on computer vision and pattern recognition*, 3883–3891.
- Ortiz, A.; Robinson, C.; Morris, D.; Fuentes, O.; Kiekintveld, C.; Hassan, M. M.; and Jovic, N. 2020. Local context normalization: Revisiting local normalization. In *Proceedings of the IEEE/CVF Conference on Computer Vision and Pattern Recognition*, 11276–11285.
- Park, T.; Liu, M.-Y.; Wang, T.-C.; and Zhu, J.-Y. 2019. Semantic image synthesis with spatially-adaptive normalization. In *Proceedings of the IEEE/CVF Conference on Computer Vision and Pattern Recognition*, 2337–2346.
- Qin, X.; Wang, Z.; Bai, Y.; Xie, X.; and Jia, H. 2020. FFA-Net: Feature fusion attention network for single image dehazing. In *Proceedings of the AAAI Conference on Artificial Intelligence*, volume 34, 11908–11915.
- Shen, Z.; Wang, W.; Lu, X.; Shen, J.; Ling, H.; Xu, T.; and Shao, L. 2019. Human-aware motion deblurring. In *Proceedings of the IEEE/CVF International Conference on Computer Vision*, 5572–5581.
- Suin, M.; Purohit, K.; and Rajagopalan, A. 2020. Spatially-attentive patch-hierarchical network for adaptive motion deblurring. In *Proceedings of the IEEE/CVF Conference on Computer Vision and Pattern Recognition*, 3606–3615.
- Ulyanov, D.; Vedaldi, A.; and Lempitsky, V. 2016. Instance normalization: The missing ingredient for fast stylization. *arXiv preprint arXiv:1607.08022*.
- Wang, T.; Yang, X.; Xu, K.; Chen, S.; Zhang, Q.; and Lau, R. W. 2019. Spatial attentive single-image deraining with a high quality real rain dataset. In *Proceedings of*

the *IEEE/CVF Conference on Computer Vision and Pattern Recognition*, 12270–12279.

Woo, S.; Park, J.; Lee, J.-Y.; and Kweon, I. S. 2018. Cbam: Convolutional block attention module. In *Proceedings of the European conference on computer vision (ECCV)*, 3–19.

Wu, T.; Tang, S.; Zhang, R.; Cao, J.; and Zhang, Y. 2020. Cgnet: A light-weight context guided network for semantic segmentation. *IEEE Transactions on Image Processing*, 30: 1169–1179.

Wu, Y.; and He, K. 2018. Group normalization. In *Proceedings of the European conference on computer vision (ECCV)*, 3–19.

Yi, Q.; Li, J.; Dai, Q.; Fang, F.; Zhang, G.; and Zeng, T. 2021. Structure-Preserving Deraining with Residue Channel Prior Guidance. In *IEEE International Conference on Computer Vision*.

Yu, T.; Guo, Z.; Jin, X.; Wu, S.; Chen, Z.; Li, W.; Zhang, Z.; and Liu, S. 2020. Region normalization for image inpainting. In *Proceedings of the AAAI Conference on Artificial Intelligence*, volume 34, 12733–12740.

Zamir, S. W.; Arora, A.; Khan, S.; Hayat, M.; Khan, F. S.; Yang, M.-H.; and Shao, L. 2020. CycleISP: Real Image Restoration via Improved Data Synthesis. In *CVPR*.

Zamir, S. W.; Arora, A.; Khan, S.; Hayat, M.; Khan, F. S.; Yang, M.-H.; and Shao, L. 2021a. Multi-Stage Progressive Image Restoration. In *CVPR*.

Zamir, S. W.; Arora, A.; Khan, S.; Hayat, M.; Khan, F. S.; Yang, M.-H.; and Shao, L. 2021b. Multi-Stage Progressive Image Restoration. *arXiv preprint arXiv:2102.02808*.

Zhang, H.; Wu, C.; Zhang, Z.; Zhu, Y.; Zhang, Z.; Lin, H.; Sun, Y.; He, T.; Muller, J.; Manmatha, R.; Li, M.; and Smola, A. 2020. ResNeSt: Split-Attention Networks. *arXiv preprint arXiv:2004.08955*.

Zhang, Y.; Li, K.; Li, K.; Wang, L.; Zhong, B.; and Fu, Y. 2018. Image super-resolution using very deep residual channel attention networks. In *Proceedings of the European conference on computer vision (ECCV)*, 286–301.

## Appendices

In this document, we provide details of our implementations (Sec. A) for better reproducibility and additional visualized results (Sec. B) of our approach and existing methods.

### Appendix A Reproducibility

In this section, we provide the details (e.g. architecture, datasets, training and testing details) of all experiments (baseline in Sec. A.1, image restoration tasks in Sec. A.2 and segmentation tasks in Sec. A.3). In addition, we also provide the hyperparameter tuning range in Sec. A.4 and computing infrastructure in Sec. A.5.

| input size        | learning rate      | batch size | # iterations |
|-------------------|--------------------|------------|--------------|
| $128 \times 128$  | $4 \times 10^{-4}$ | 256        | 300000       |
| $256 \times 256$  | $4 \times 10^{-4}$ | 64         | 300000       |
| $384 \times 384$  | $9 \times 10^{-4}$ | 64         | 133333       |
| $512 \times 512$  | $4 \times 10^{-4}$ | 16         | 300000       |
| $720 \times 1280$ | $7 \times 10^{-4}$ | 8          | 170667       |

Table 5: Hyper-parameters when training with different input size.

### A.1 Implementation Details for Baseline

We do quantity experiments and ablation studies on Go-Pro (Nah, Hyun Kim, and Mu Lee 2017) dataset and the implementation details will be described in this subsection.

**Architecture** We use a simple UNet model (i.e. HINet Simple (Chen et al. 2021a) without HIN) as baseline to reduce the interference caused by advanced modules or model architectures.

Attention modules (e.g., SE (Hu, Shen, and Sun 2018), GE- $\theta^-$  (Hu et al. 2018) and CBAM (Woo et al. 2018)) are added to the encoder of UNet following (Hu, Shen, and Sun 2018). In detail, block is integrated into residual block and place after the residual unit but before the summation with the identity branch. Attention modules are added to all residual blocks in encoder of UNet.

Normalization modules (e.g., IN (Ulyanov, Vedaldi, and Lempitsky 2016) and GN (Wu and He 2018)) are added to the UNet following HINet (Chen et al. 2021a). In detail, both IN and GN are extended to Half-IN and Half-GN respectively, and are placed after the first convolution layer but before activation layer in residual blocks. Following (Chen et al. 2021a), normalization modules are only added to the last two stages of the encoder of UNet.

**Training** We follow the most training detail of HINet Simple (Chen et al. 2021a) except training patch size and batch size. The models are trained with Adam optimizer. The learning rate is set to  $4 \times 10^{-4}$  by default, and decreased to  $1 \times 10^{-7}$  with cosine annealing strategy (Loshchilov and Hutter 2016). In default, the models are trained on  $256 \times 256$  patches with a batch size of 64 for  $3 \times 10^5$  iterations. When training with other input sizes, we keep the total number of pixels seen by the model during training the same as the default configuration for a fair comparison. Other hyper-parameters are adjusted based on experimental trials and the details are shown in Tab. 5. In addition, we also use the warm-up strategy in the first 5000 iterations, where the learning rate grows linearly from 0 to the initial learning rate, to alleviate the training instability caused by the large learning rate at the beginning of training. Flip and rotation are also used as data augmentation.

### A.2 Implementation Details for Applications on Existing Image Restoration tasks

To verify the effectiveness of the proposed TLSC, we apply it to various existing models for image restoration. In this subsection, we will briefly describe the existing methods and

the details of our implementations. It is worth emphasizing that our approach can utilize existing trained model (if publicly available) without retraining or finetuning.

**Deblurring** We apply TLSC with HINet (Chen et al. 2021a) and MPRNet (Zamir et al. 2021a) and evaluate them on test set of GoPro (Nah, Hyun Kim, and Mu Lee 2017), HIDE (Shen et al. 2019) and REDS (Nah et al. 2019) dataset. All this three datasets contains images with size of  $720 \times 1280$ . And the MPRNet and HINet are trained with patches with size of  $256 \times 256$ . The size of local window for TLSC is set to  $384 \times 384$ .

**GoPro (Nah, Hyun Kim, and Mu Lee 2017)** We directly use the publicly available HINet (Chen et al. 2021a) and MPRNet (Zamir et al. 2021a) trained by GoPro (Nah, Hyun Kim, and Mu Lee 2017).

**HIDE (Shen et al. 2019)** Following (Zamir et al. 2021a), we take GoPro trained model and directly apply it on the test images of the HIDE (Shen et al. 2019). The HIDE (Shen et al. 2019) dataset is specifically collected for human-aware motion deblurring and its test set contains 2,025 images.

**REDS (Nah et al. 2019)** Since HINet and MPRNet trained by REDS (Nah et al. 2019) are not publicly available, we train HINet on REDS dataset with jpeg compression artifacts. The training detail is following (Chen et al. 2021a) and we evaluate the results on REDS-val-300.

**Dehazing** Feature fusion attention network (FFA-Net) (Qin et al. 2020) is a model for single image dehazing. FFA-Net was trained with  $240 \times 240$  patches from image dehazing benchmark RESIDE (Li et al. 2018a), which contains synthetic hazy images in both indoor and outdoor scenarios. We test the results on Synthetic Objective Testing Set (SOTS) from RESIDE (Li et al. 2018a) dataset, which contains 500 indoor images and 500 outdoors ones. The size of local window is set to  $480 \times 480$  and  $416 \times 416$  for SOTS (indoor) and SOTS (outdoor) respectively.

**Deraining** Structure-Preserving Deraining Network (SPDNet) (Yi et al. 2021) is a top-performing model for deraining task. SPDNet was trained on SPA-Data (Wang et al. 2019) with patch size of  $128 \times 128$ . SPA-Data (Wang et al. 2019) is a real-world deraining dataset which contains 28,500 and 1,000 rain/clean image pairs with size of  $512 \times 512$  for training and testing respectively. The size of local window is set to  $384 \times 384$ .

### A.3 Implementation Details for Semantic Segmentation

We also test our approach in semantic segmentation tasks and the implementation details will be described in this subsection.

**Dataset** The Cityscapes (Cordts et al. 2016) is one of the widely-used datasets for semantic segmentation. It has 5,000 high quality pixel-level finely annotated images captured from 50 different cities, with 2,975 for training, 500 for validation and another 1,525 for testing. In total there are 30 semantic classes provided, 19 of which are used for evaluation. The standard mean Intersect over Union (mIoU) on the

validation set is reported for measuring segmentation accuracy.

**Implement Details** We apply TLSC to CGNet (Wu et al. 2020) and ResNeSt (Zhang et al. 2020), such that the global average pooling layers in this backbones are replaced by local average pooling layers. We utilize the implementation from mmsegmentation (Contributors 2020). All models are trained with  $512 \times 1024$  cropped images and testing with  $1024 \times 2048$  full-images. The size of local window for TLSC is set as i.e.  $512 \times 1024$ , which is equal to input size for training. We use the public available checkpoints from mmsegmentation (Contributors 2020). MACs is calculated with input size  $1024 \times 2048$ .

**CGNet (Wu et al. 2020).** Context Guided Network (CGNet (Wu et al. 2020)) is a lightweight and efficient network for semantic segmentation. We use the checkpoint trained by mmsegmentation (Contributors 2020) with crop size  $512 \times 1024$ .

**ResNeSt (Zhang et al. 2020)** ResNeSt backbone, which is a variant of ResNet (He et al. 2016), with Split-Attention blocks. We use ResNeSt-101 as backbone and DeepLabV3+ (Chen et al. 2018) as segmentation decoder.

### A.4 The Hyperparameter Tuning Range

Size of local window is a hyper-parameter for our approach (TLSC). For TLSC applied for MPRNet and HINet, the size of local window is chosen from  $\{256 \times 256, 384 \times 384, 512 \times 512, 720 \times 720\}$ . For TLSC applied for FFANet, the size of local window is chosen from  $\{128 \times 128, 256 \times 256, 384 \times 384, 512 \times 512\}$ . For TLSC applied for SPDNet, the size of local window is chosen from  $240 \times 240$  to  $480 \times 480$  with stride  $16 \times 16$ . For TLSC applied for all models on segmentation tasks, we simply use the size  $512 \times 1024$ , which is equal to the size of training patches.

### A.5 Computing Infrastructure

All the experiments are conducted on Nvidia RTX 2080Ti GPUs (11GB memory). Other configuration includes Intel(R) Xeon(R) Gold 6130 CPU @ 2.10GHz, 384GB DDR4 RAM and 1TB hard drive (HDD), which is sufficient for all the baselines. We use 8 GPUs for training, while only 1 GPU was needed for testing.

## Appendix B Visualized Results

In this section, we provide additional visual results of statistics distribution (Sec. B.1), boundary artifacts (Sec. B.2) and qualitative comparisons between our approach and existing methods (Sec. B.3).

### B.1 Statistics Distribution

We provide more results of statistics distribution between training and testing on GoPro (Nah, Hyun Kim, and Mu Lee 2017) dataset. Statistics aggregated by HINet (Chen et al. 2021a) are shown in Fig. 7. Statistics aggregated by MPRNet (Zamir et al. 2021a) are shown in Fig. 8. For both HINet (Chen et al. 2021a) and MPRNet (Zamir et al. 2021a), the statistics distribution shifts from training (green) to testing (blue). The statistics distribution shifts is reduced by

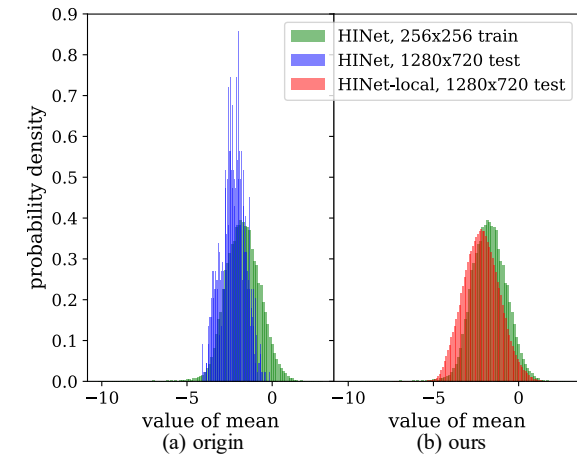
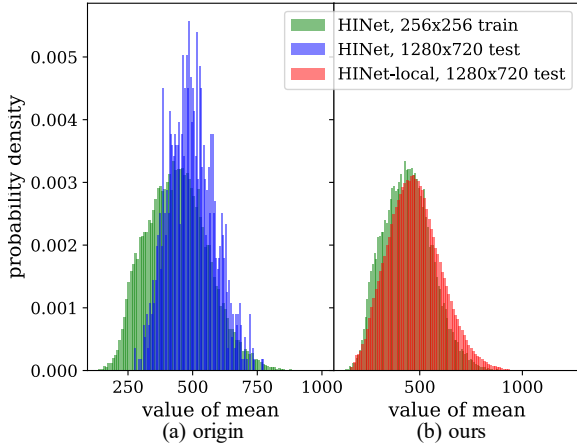


Figure 7: Visualization of the statistics (mean) distribution of Instance Normalizations (Ulyanov, Vedaldi, and Lempit-sky 2016) in HINet (Chen et al. 2021a) on GoPro dataset. Green: the distribution when training with patches; Blue: the distribution when testing with images; Red: the distribution when testing with images and TLSC is adopted (denoted as HINet-local). (a) The original test scheme results in distribution shifts. (b) Distribution shifts could be reduced by our proposed TLSC.

TLSC as shown in Fig. 7b and Fig. 8b compares to Fig. 7a and Fig. 8a: the statistics distribution obtained by our HINet-local/MPRNet-local (red) is close to the original HINet/MPRNet in the training phase (green).

## B.2 Boundary Artifacts

Cropping the image into patches and predict the result independently induces unsmoothness of the boundary (i.e. “boundary artifacts” as demonstrated in (Lee 2015)). We give some example images of block boundary artifacts in Fig. 9, which are generated by MPRNet (Zamir et al. 2021b) on GoPro (Nah, Hyun Kim, and Mu Lee 2017) dataset. There

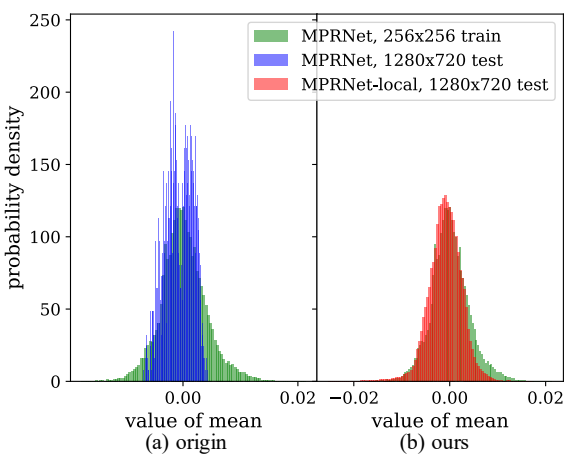
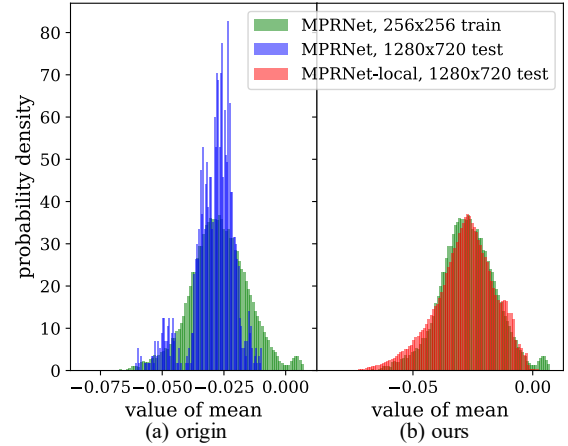


Figure 8: Visualization of the statistics (mean) distribution of SE (Hu, Shen, and Sun 2018) layers in MPRNet on GoPro dataset. Green: the distribution when training with patches; Blue: the distribution when testing with images; Red: the distribution when testing with images and TLSC is adopted (denoted as MPRNet-local). (a) The original test scheme results in distribution shifts. (b) Distribution shifts could be reduced by our proposed TLSC.

are obvious boundary artifacts in Fig. 9 which seriously degrades the quality of the image.

## B.3 Qualitative Comparisons

In this section, provide additional qualitative results on various image restoration tasks (e.g. deburring, deraining and dehazing) for qualitative comparisons.

**Deburring** We give the comparison of the visual effect in Fig. 10 and Fig. 10 for qualitative comparisons. Compared to the original MPRNet (Zamir et al. 2021b) which test with patches (Fig. 10b and Fig. 10b), our approach (Fig. 10d and Fig. 10d) restores high quality images without boundary artifacts. Compared to the original MPRNet (Zamir et al.

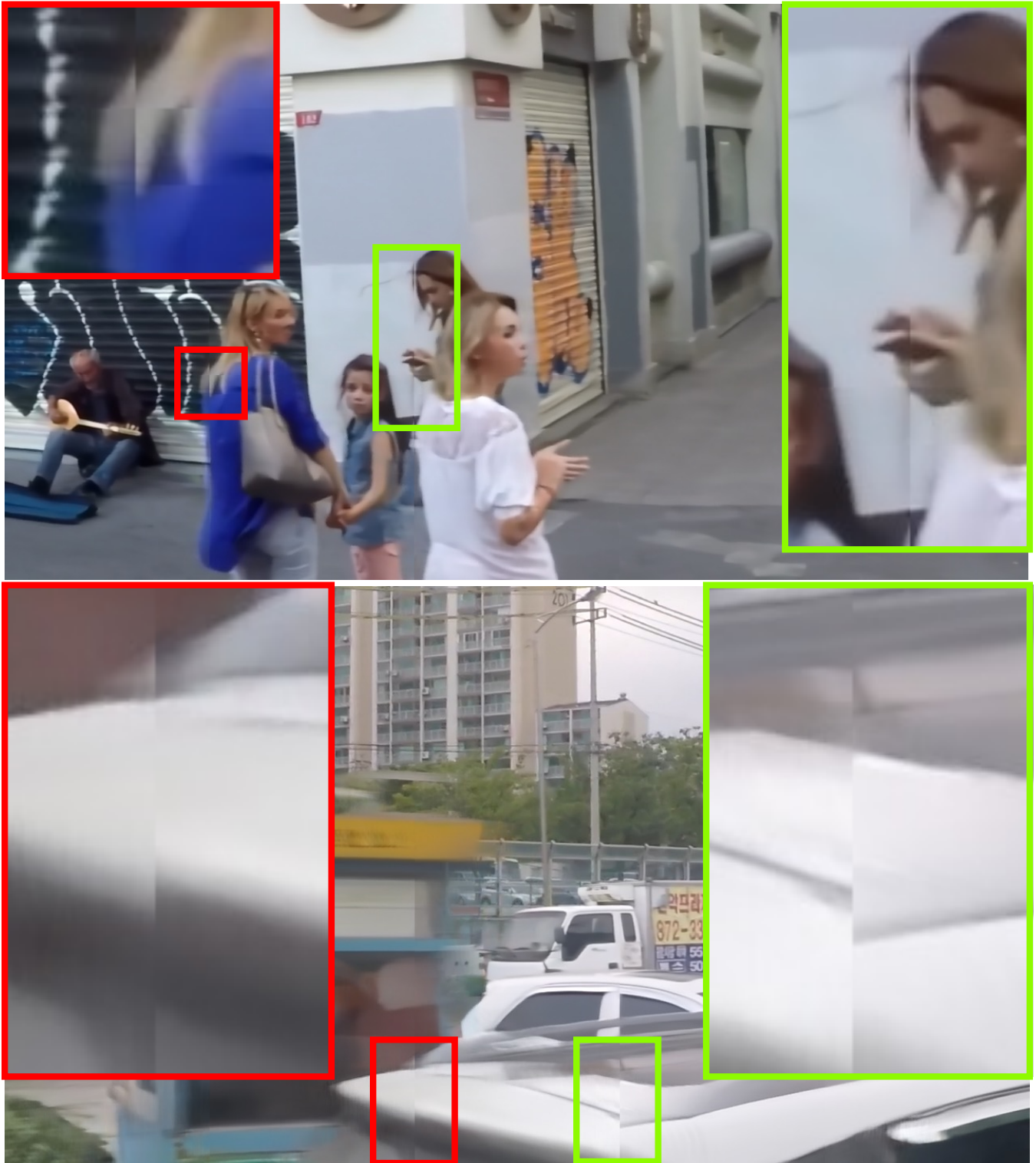


Figure 9: Deblurring results of MPRNet (Zamir et al. 2021b) on GoPro (Nah, Hyun Kim, and Mu Lee 2017) when testing with patches. They introduce visible artifacts at patch boundaries, which look like there are vertical stripes cutting through the picture.

2021b) which test with images (Fig. 10c and Fig. 10c), our approach (Fig. 10d and Fig. 10d) restores clearer and sharper images.

**Deraining** We give the comparison of the visual effect in Fig. 12 for qualitative comparisons. Compared to the original SPDNet (Zamir et al. 2021b), our approach restores clearer images.

**Dehazing** We give the comparison of the visual effect in Fig. 13 for qualitative comparisons. We also test the results on Realistic Hazy Images for subjective assessment in Fig. 14. Compared to the original FFANet (Zamir et al. 2021b), our approach restores clearer images.



(a) Blurry Image (PSNR)



(b) origin + patches (29.02dB)

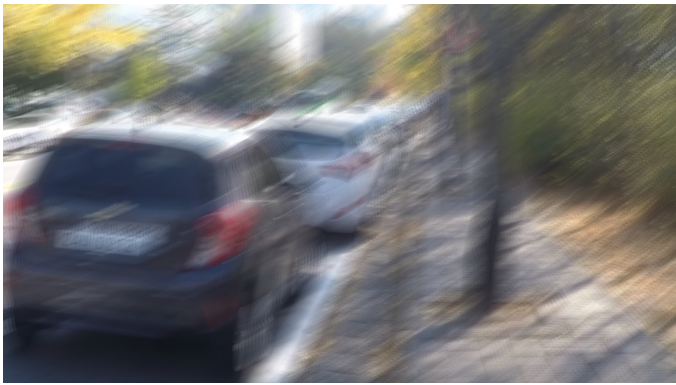


(c) origin + full-image (29.87dB)



(d) ours + full-image (30.70dB)

Figure 10: Deblurring results of MPRNet (Zamir et al. 2021b) on GoPro (Nah, Hyun Kim, and Mu Lee 2017) generated by different testing schemes. **Left:** full-images. **Right:** crops from left image. (b) Test with patches; (c) Test with images; (d) Test with images and TLSC is adopted (ours). It illustrates that (d) provides sharper results than (c) while avoids the boundary artifacts in (b).



(a) Blurry Image (PSNR)



(b) origin + patches (25.55dB)



(c) origin + full-image (25.67dB)



(d) ours + full-image (27.03dB)

Figure 11: More deblurring results of MPRNet (Zamir et al. 2021b) on GoPro (Nah, Hyun Kim, and Mu Lee 2017) generated by different testing schemes. The table notes are consistent with Fig. 10.

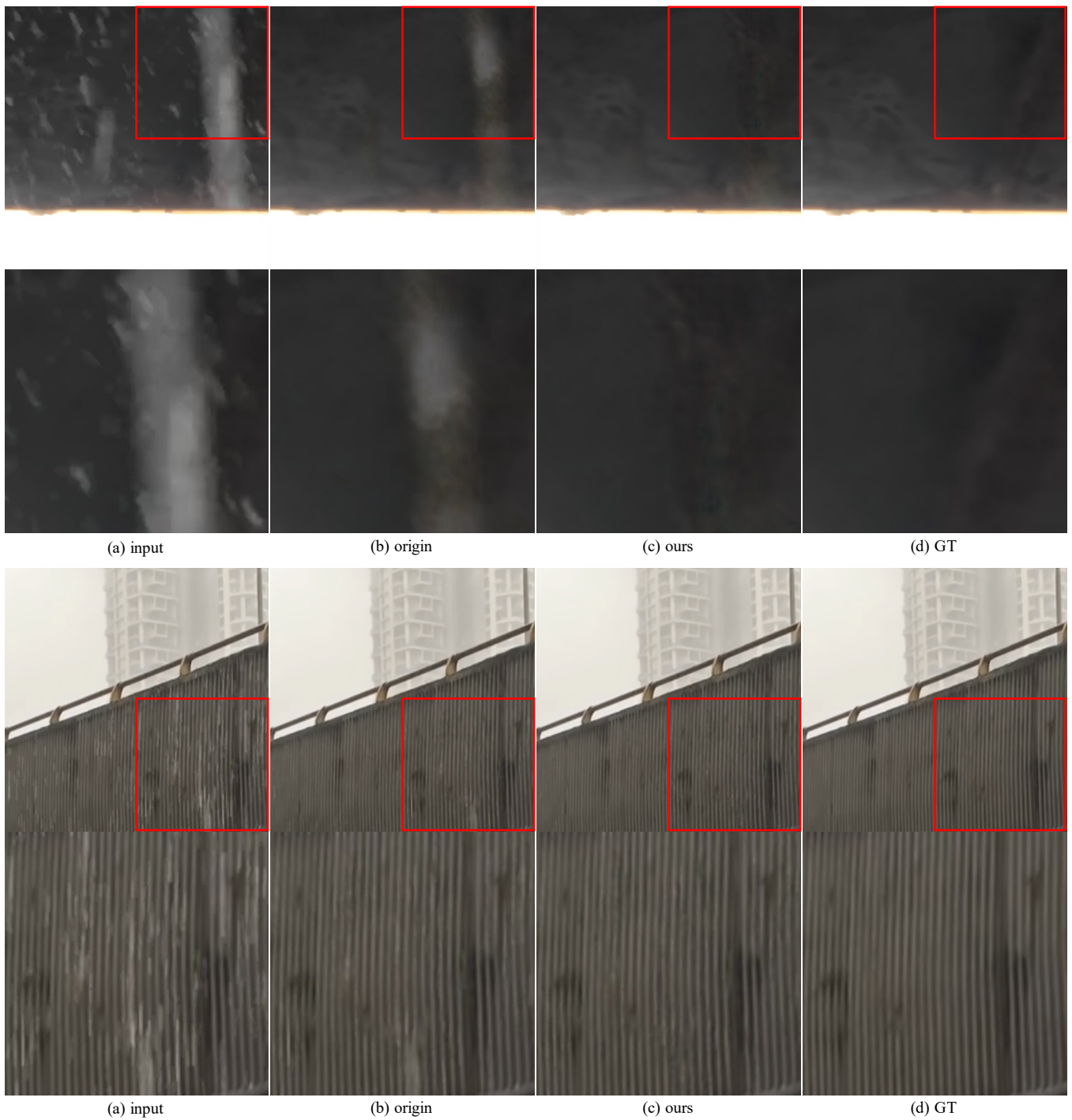


Figure 12: Deraining results of SPDNet (Yi et al. 2021) on SPA-Data (Wang et al. 2019) dataset generated by different testing methods. (a) Rainy images as inputs. (b) Results based on full-image produced by the original SPDNet. Some of the rainwater in images is not removed cleanly. (c) Results based on full-image produced by SPDNet with the proposed TLSC, which are clearer. (d) Ground truth for reference.

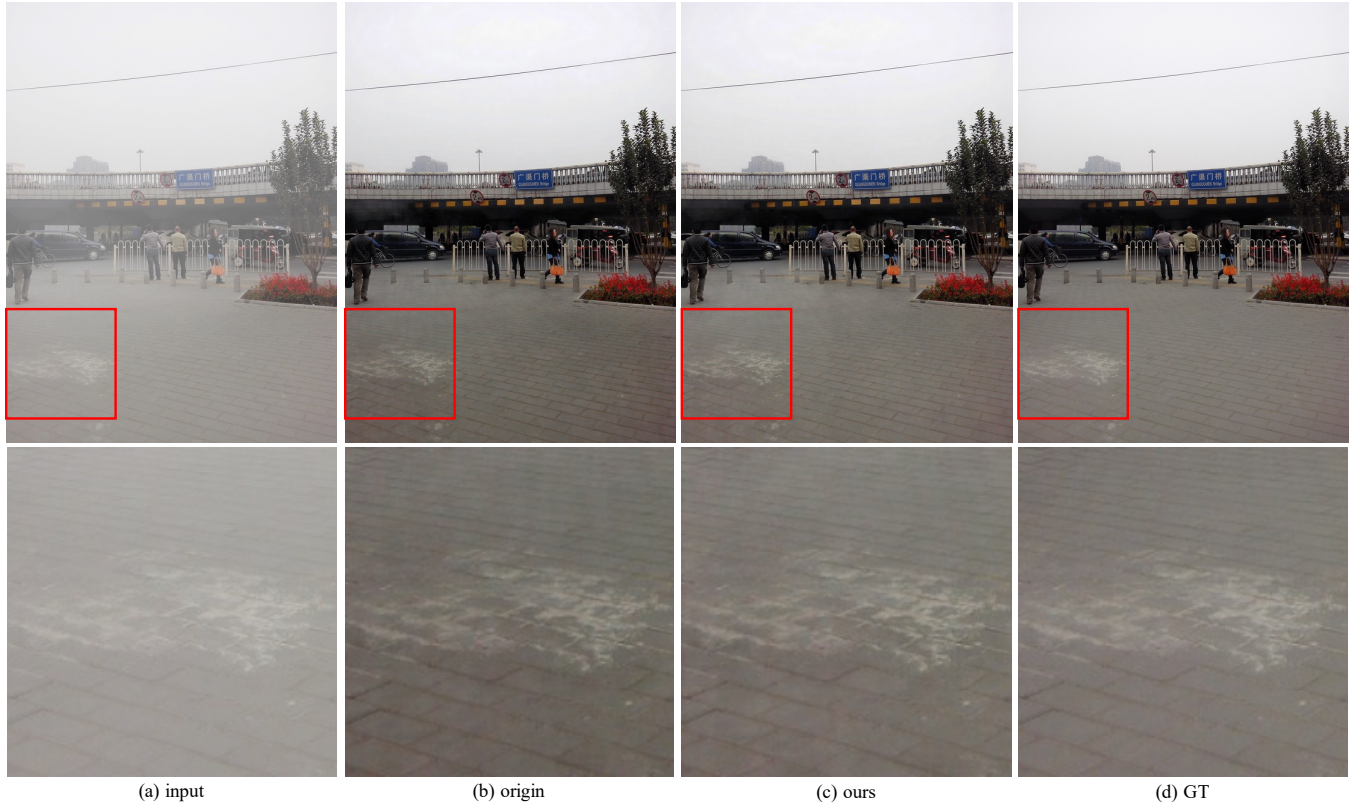


Figure 13: Dehazing results of FFANet (Qin et al. 2020) on Synthetic Objective Testing Set (SOTS) from RESIDE (Li et al. 2018a) dataset generated by different testing methods. (a) Hazy images as inputs. (b) Result based on full-image produced by the original FFANet. The image is gray with obvious noise. (c) Result based on full-image produced by FFANet with the proposed TLSC, which is brighter with fewer noises. (d) Ground truth for reference.

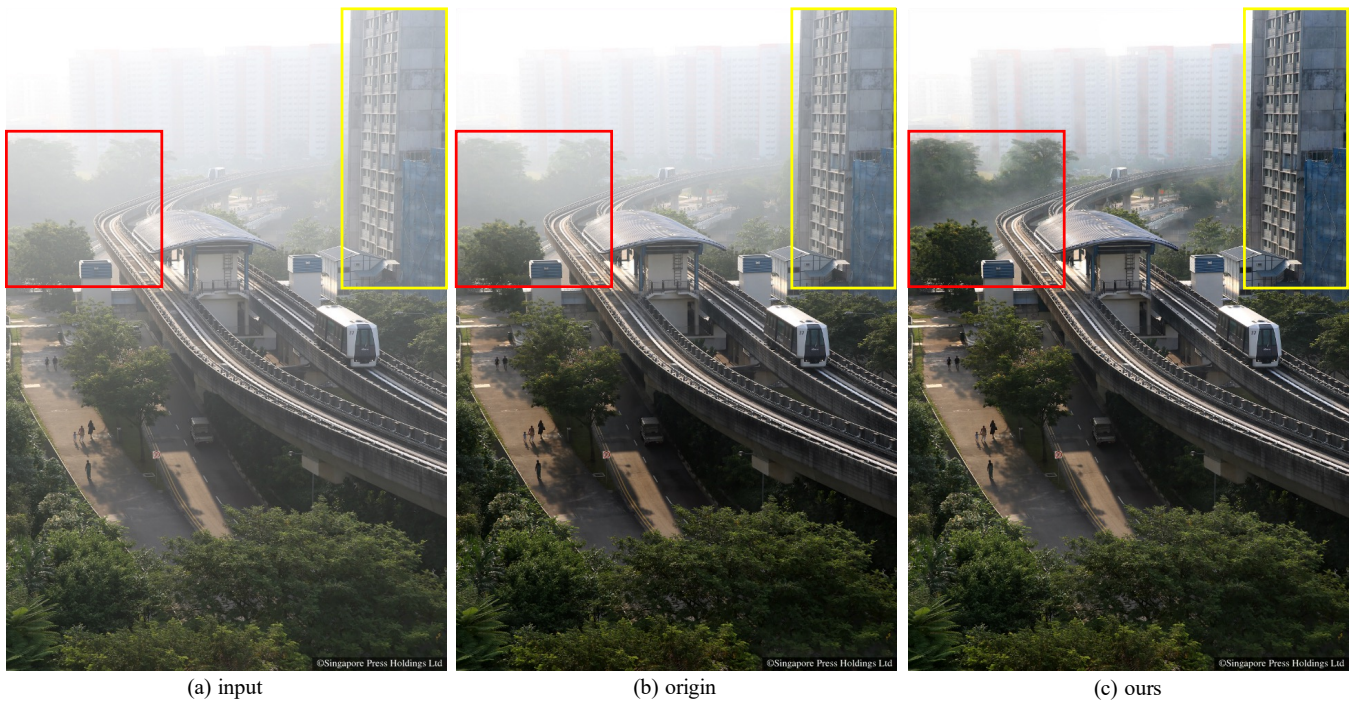


Figure 14: Qualitative comparisons on Realistic Hazy Image. Dehazing results are generated by FFANet (Qin et al. 2020) with different testing methods. (a) Realistic hazy images as inputs. (b) Result based on full-image produced by the original FFANet. The trees and buildings in the distance are still hazy. (c) Result based on full-image produced by FFANet with the proposed TLSC, which is cleaner.